RESEARCH ARTICLE | AUGUST 09 2024

Topology during magnetic reconnection events in RFX-mod

P. Porcu ; G. Spizzo ; M. Veranda ; M. Zuin ; M. Agostini ; M. Gobbin ; D. Terranova ; RFX-mod Team

Phys. Plasmas 31, 082506 (2024)
https://doi.org/10.1063/5.0211018

Topology during magnetic reconnection events in RFX-mod

Cite as: Phys. Plasmas **31**, 082506 (2024); doi: 10.1063/5.0211018
Submitted: 28 March 2024 · Accepted: 13 July 2024 ·
Published Online: 9 August 2024

P. Porcu,[1,2,a)] G. Spizzo,[2,3] M. Veranda,[2,3] M. Zuin,[2,3] M. Agostini,[2,3] M. Gobbin,[2,3] D. Terranova,[2,3] and RFX-mod Team[b)]

AFFILIATIONS

[1]Centro Ricerche Fusione - University of Padova, c/o Consorzio RFX, C.so Stati Uniti 4, 35127 Padova, Italy
[2]Consorzio RFX (CNR, ENEA, INFN, Università di Padova, Acciaierie Venete SpA), C.so Stati Uniti 4, 35127 Padova, Italy
[3]Istituto per la Scienza e la Tecnologia dei Plasmi del CNR, C.so Stati Uniti 4, 35127 Padova, Italy

[a)]**Author to whom correspondence should be addressed:** pasquale.porcu@igi.cnr.it
[b)]See the author list of Marrelli *et al.*, Nucl. Fusion, **59**, 076027 (2019).

ABSTRACT

This paper is devoted to the characterization of magnetohydrodynamics (MHD) tearing modes causing plasma–wall interaction (PWI) in the Reversed-Field eXperiment (RFX-mod) reversed-field pinch (RFP) device. We study an example of a magnetic reconnection event in a high plasma current discharge. The PWI is measured via a fast camera looking at the graphite-covered inner wall, showing two separated footprints of neutral carbon radiation. A first, simple analysis shows that the phase-locking of $m = 1$ tearing modes is the principal cause of enhanced PWI, as it is well documented in literature. Many modes contribute to the phase-locking, actually more than those measured with the magnetic sensors. A more refined analysis is based on calculation of the Connection Length to the wall and of the loss time of Maxwellian ions via the Hamiltonian guiding center code ORBIT. This analysis confirms the importance of the $m = 1$ phase-locking as a loss channel of high-energy particles, which is the mechanism that dominates the PWI pattern, but an additional role of the $m = 0$, $n = 7$ mode is highlighted, which is a new result for the RFP. The PWI mediated by the $m = 0$ islands is milder, which is a good outlook for the RFX-mod2 upgraded device, currently in the assembly phase.

I. INTRODUCTION

The Reversed-Field eXperiment (RFX-mod) is a medium-sized device that was operated at Consorzio RFX, in Padova (Italy) between 2004 and 2015.[1] It was an improved version of the old RFX[2] (1991–1999). RFX-mod has a major radius $R_0 = 2$ m and a minor radius $a = 0.459$ m. It mainly works in the so-called reversed-field pinch (RFP) magnetic configuration for plasma confinement.[3] RFX-mod is devoted to the study of the RFP confinement at high plasma current ($I_p \leq 2$ MA) and the active control of magnetohydrodynamics (MHD) instabilities. Presently, the device is being upgraded and will resume operations as a new modified version, named RFX-mod2,[4] by the end of 2025.

In the RFP, the safety factor $q(r)$ is monotonically decreasing with minor radius, it vanishes at the plasma edge and becomes slightly negative at the wall. The surface with $q = 0$ is called "reversal surface." As a consequence, a large number of MHD modes can resonate with mode numbers $m = 1$, $n > n_0$, where the value of n_0 depends on the q profile, as shown in Fig. 1.

The numbers m and n represent the poloidal and the toroidal periodicity of the magnetic field line and correspond to the number of magnetic islands along the respective angles θ and φ. In RFX-mod, the value of the on-axis safety factor, $q(0) = \lim_{r\to 0}(rB_\varphi)/(R_0 B_\theta) \approx 0.15$, which is rather small with respect to the tokamak due to the large value of B_θ. As a consequence, the innermost $m = 1$ resonant mode has toroidal mode number $n_0 = 7$. In addition to $m = 1$ modes, the presence of the reversal surface causes the resonance of the $m = 0$, $n \geq 1$ spontaneous tearing mode instabilities.[5]

The $m = 1$ mode spectrum is characterized by rich dynamics[7] showing a typical interplay between modes. The scenario where the innermost (dominant) $n_0 = 7$ mode prevails in the spectrum with an amplitude much larger than the other $n > 7$ modes, dubbed "secondary" modes, is called quasi-single helicity (QSH) state. Plasma in the QSH state is characterized by enhanced confinement properties and an ordered topology. The QSH was initially discovered in RFX,[8,9] but then it was found in several other RFPs,[10–13] confuting the

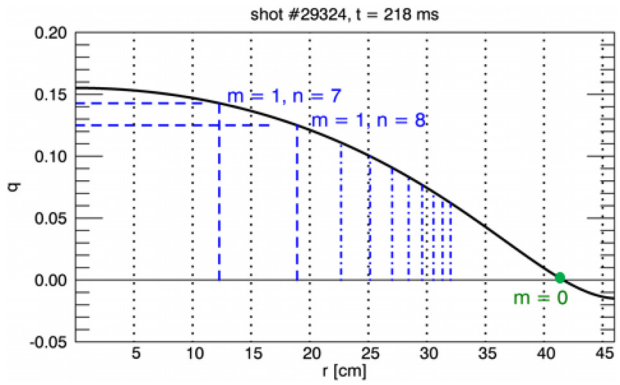

FIG. 1. Safety factor profile in a typical, high current RFX-mod discharge. The innermost resonances with $m = 1$, $n = 7, 8$ are marked as vertical, dashed lines. The $m = 0$ modes resonate at the reversal surface, where q vanishes (green dot).

paradigm, based on the Taylor's theory,[14] that the RFP was always dominated by magnetic chaos.[15] When no mode dominates, the spectrum is broad[16–18] and the plasma is in the traditional, chaotic, low-confinement state called multiple helicity (MH).[5] QSH states are found more often when running high plasma current discharges,[9,18] due to the favorable scaling with the Hartmann number.[19] QSH states at high current are nevertheless interrupted by reconnection events, which drive the system to the MH:[6,20] these events are also called "crashes." The interest in crashes is both theoretical, since they are very interesting examples of magnetic reconnection events,[21,22] and practical, since they are associated with the loss of confinement, marking the transition from the good QSH phase to short hiatuses when the mode spectrum is in the MH. The transition is characterized by a sudden, total or partial decrease in the dominant mode amplitude and the consequent rapid growth of secondary modes. A typical example of a QSH-MH transition is reported in Fig. 2, which shows how the plasma parameters change during the reconnection event (crash): the $m = 1$, $n = 7$ amplitude (black) decreases and the r.m.s. of the secondary modes (red) increases at the same time. Regarding magnetic equilibrium, the toroidal and the poloidal components are subject to a sudden change, which is traditionally monitored through the so-called "reversal" and "pinch" parameters, F and Θ. They are defined according to[23]

$$F = \frac{B_\varphi(a)}{\langle B_\varphi \rangle}, \quad \Theta = \frac{B_\theta(a)}{\langle B_\varphi \rangle}, \tag{1}$$

where $B_\varphi(a)$ and $B_\theta(a)$ represent the toroidal and poloidal magnetic field strengths at the edge. Brackets, $\langle \cdot \rangle$, indicate the radial average of the profile. Figure 2(b) shows that Θ increases during the QSH phase, which indicates that the parallel current peaks on axis,[23] while during the crash F drops, meaning that the current profile is flattened and the toroidal component becomes more "reversed."[24] The main consequence of this global redistribution of the equilibrium fields is the weakening of magnetic confinement.[20] This can be easily observed in Figs. 2(d) and 2(e), showing the core electron temperature and the electron density both in the core and at the edge ($r/a \approx 0.9$). As expected, the plasma core cools down since the "Internal Transport Barrier" (ITB) associated with QSH[9,25] disappears, partially or

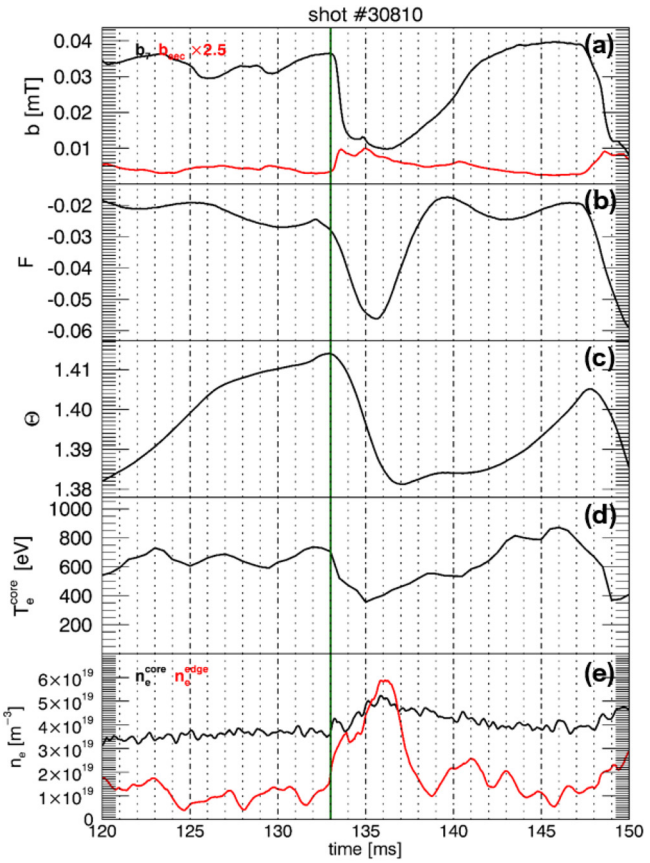

FIG. 2. QSH-MH cycle during RFX-mod shot #30810, at $t = 133$ ms. (a) $m = 1$ mode amplitude, b, during discharge #29324. b_7 (black) represents the dominant 1,7 mode amplitude, b_{sec} (red) indicates the r.m.s. of the secondary mode amplitudes, (b) reversal parameter F, (c) pinch parameter Θ, (d) core electron temperature, and (e) core electron density (black) and edge electron density (red). Crash time instant is marked with a vertical, dark green line. Adapted from Ref. 6.

completely. At the same time, the edge density increases [Fig. 2(e)], which is a signature of particle loss and enhanced wall recycling.

As already shown in Fig. 2(a), during the crash, secondary modes grow in amplitude. In addition to this, they also tend to align their phases: the main consequence is the development of a strong toroidally localized plasma deformation, called Slinky or Locked Mode (LM).[26,27] Experimentally, the LM is the cause of particle losses associated with strong plasma–wall interaction (PWI),[28] overheating of the plasma facing components,[29,30] sputtering,[31] and radiation.[32,33] All of these must be avoided or mitigated in the future RFX-mod2 upgrade.

This paper deals with an example of a crash happening in the discharge #29324, characterized by high plasma current: $I_p \approx 1.6$ MA at the flat top. The discharge is mainly in the QSH state; nevertheless, several crashes are observed. From Fig. 3(a), we noticed that one of these crashes happens at $t = 218$ ms and determines a well diagnosed PWI event.[33] In fact, Fig. 3(c) was taken by a charge-coupled device (CCD) camera looking at the inner wall of the device,[34] showing two separated footprints, located toroidally at $\varphi_0 = -8°$ and $\varphi_1 = 7°$. The vacuum vessel of RFX-mod is protected against the edge plasma with graphite

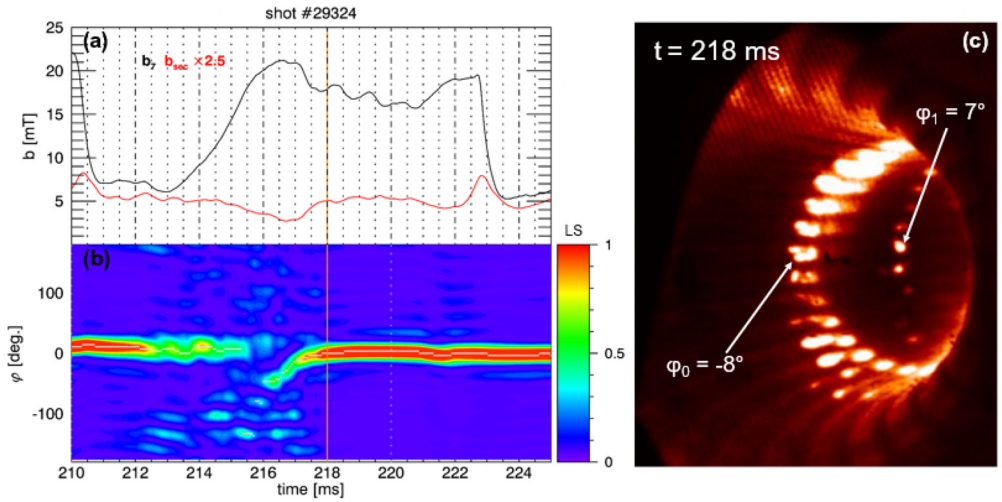

FIG. 3. (a) $m = 1$ mode amplitude, b, during discharge #29324. b_7 (black) represents the dominant 1,7 mode amplitude, b_{sec} (red) indicates the r.m.s. of the secondary mode amplitudes. Time instant $t = 218$ ms is marked with a vertical, orange line. (b) Locked-Mode shape, described by using the Locking Strength parameter with modes $8 \leq n \leq 23$. (c) Image of the PWI in the same shot and time instant. Adapted from Ref. 33. The two red footprints are located toroidally at $\varphi_0 = -8°$ and $\varphi_1 = 7°$.

tiles, which completely cover the first wall.[35] Therefore, the PWI pattern is detected by looking at the CI (neutral carbon) emission line at 970 nm. In Fig. 3(a), it is noteworthy that the QSH survives despite the crash: this is not uncommon, most reconnection events may not destroy the QSH state completely, and thus they are dubbed "minor crashes."[20]

The contour map in Fig. 3(b) shows the evolution of the toroidal position of the LM, which was located at $\varphi \approx 0$ during the crash. The LM toroidal position is determined by using the "Locking Strength" (LS),[17,36] a parameter that quantifies the level of $m = 1$ mode alignment: LS = 1 means complete phase-locking, while LS = 0 means random phases. From Fig. 3(b), it follows that maximum PWI is found at the locking position, which is a well-known result in the RFP.[29–31,33] In fact, in the old RFX device, PWI was dominated by the LM, which was also locked to the wall: measurements scaled with the LM position, no refined analysis was necessary.[28,29,31,32] In the RFX-mod upgrade, the LM was put into rotation, and considerably reduced in size: the role of $m = 0$ modes in determining the PWI was discovered and described with more accurate numerical methods, e.g., the deformation of the last closed flux surface (LCFS).[30] With the progress in the exploitation of the feedback system,[37] and the exploration of the high current scenario,[18] the QSH state started to dominate the PWI,[38–40] and the LM had a role only during the crashes,[20,33] as explained above. This new scenario requires to develop nonlinear, numerical methods characterized by much more detail with respect to what was done in the past: this is the goal of the present paper. The methods proposed here could be of some interest also for the tokamak community, since phase-locking of the $m = 2$, $n = 1$ and $m = 3$, $n = 1$ modes is often seen in tokamaks,[41] and ensuing stochasticity has been proposed as an important mechanism prior to disruptions.[42,43]

In the paper, a gradual approach of increasing complexity will be used. First, it is possible to calculate the plasma deformation induced by the LM of the $m = 1$, $n > 7$ modes, following the traditional method of the LCFS used in RFX-mod.[30] This is done in Sec. II. The new, more refined analysis consists in simulating the dynamics of a large number of ions in the presence of an extended spectrum of magnetic perturbations. In this paper, we calculate the Connection Length to the wall $L_{c,w}$, a metric that is widely used in the tokamak community when dealing with an ergodic magnetic edge.[44,45] To perform the calculation, in Sec. III we make use of the Hamiltonian guiding center code ORBIT,[46] and we compare the $L_{c,w}$ map with the CCD image of Fig. 3(c). Finally, to assess the impact of the various topological structures on the measured PWI, simulations with a realistic Maxwellian ion energy distribution are discussed in Sec. IV. Conclusions and final considerations are then drawn in Sec. V.

II. PLASMA SURFACE DEFORMATION INDUCED BY PHASE-LOCKING

In this section, we will analyze the deformation of the LCFS induced by the tearing modes during the crash event, following the method routinely used in RFX-mod to describe the PWI,[29,30] as explained in the Introduction. The local, ideal displacement due to a generic m, n mode can be defined as

$$\Delta_{m,n} = \mathrm{Re}\left[\frac{-i\, r b^r_{m,n}(r)\, e^{i\Phi_{m,n}(\theta,\varphi,t)}}{[m - nq(r)]B_\theta(r)}\right] = \frac{r b^r_{m,n}(r)}{[m - nq(r)]B_\theta(r)} \cos\left[\Phi_{m,n}(\theta,\varphi,t) - \frac{\pi}{2}\right], \quad (2)$$

where $b^r_{m,n}$ is the amplitude of the m, n mode, $\Phi_{m,n}$ is its global phase, q is the safety factor, and B_θ is the equilibrium poloidal magnetic field.[47,48] In RFX-mod, $\Delta_{m,n}$ is reconstructed via the NewComb Toroidal (NCT) code,[49] which solves the Newcomb's equations in toroidal geometry starting from magnetic measurements. The total LCFS deformation due to secondary modes is calculated at $r = a$ by summing linearly the individual mode contributions: $\Delta_{sec}(\theta,\varphi) = \sum_{n=8}^{23} \Delta_{1,n}(\theta,\varphi)$. We consider $m = 1$ modes, only, since they resonate in the core and the local displacement (2) does not diverge at $r = a$. On the contrary, it diverges for $m = 0$ modes because they resonate at the reversal surface, which is close to the edge, as already shown in Fig. 1.

A suitable way to describe the LCFS deformation near the LM is to define a modified version of the Dirichlet kernels that also takes into account the shape of the $m = 1$ spectrum. We call it "Locking Parameter" (LP), given by

$$\mathrm{LP}(\varphi) = \frac{1}{D}\sum_{\ell=n_{min}}^{n_{max}} A_\ell \cos(\ell\varphi), \tag{3}$$

where $D = \sum_{\ell=n_{min}}^{n_{max}} A_\ell$ is a normalization factor, in order to have maximum LP = 1 at its maximum. The LP coincides with the Locking Strength LS, if the latter is calculated on the equatorial plane at $\theta = 0$ and in the reference frame of the LM,[36] where all mode phases are equal.[48,50] The factor A_ℓ represents the weight of the ℓ-th mode in the calculation, namely, $A_\ell = n_{max} + 1 - \ell$, which reproduces well the decaying trend of the secondary $m = 1$ mode spectrum, as we will show in Sec. III D. Given that $n_{min} \equiv 8$, it follows $D = (n_{max} - 6)(n_{max} - 7)/2$ and with some algebra it follows that

$$\begin{aligned}\mathrm{LP}(\varphi) = {} & \frac{(n_{max}+1)}{(n_{max}-6)(n_{max}-7)}\left[\frac{\sin\left[\left(n_{max}+\frac{1}{2}\right)\varphi\right]}{\sin\left(\frac{\varphi}{2}\right)} - 1\right] \\ & - \frac{2\,A_{n_{max}}(\varphi)}{(n_{max}-6)(n_{max}-7)} - \frac{1}{2(n_{max}-6)(n_{max}-7)} \\ & \times \frac{(n_{max}+1)\cos(n_{max}\varphi) - n_{max}\cdot\cos[(n_{max}+1)\varphi] - 1\}}{\sin^2\left(\frac{\varphi}{2}\right)},\end{aligned} \tag{4}$$

where $A_{n_{max}} = \sum_{\ell=1}^{7}(n_{max} + 1 - \ell)\cos(\ell\varphi)$. Details about the derivation are contained in the Appendix. Such an expression for $\mathrm{LP}(\varphi)$ depends on n_{max}, which is related to the number of modes involved in the LM structure: obviously, the wider the spectrum, the more $\mathrm{LP}(\varphi)$ approximates a Dirac delta, $\delta(\varphi)$.

Figure 4 represents the comparison between the distortion of the LCFS and the $\mathrm{LP}(\varphi)$ profile taking $n_{max} = 23$: there is a correlation between the first two minima of LP and the maxima of $\Delta_{sec}(\varphi)$. Nevertheless, the distance between the two minima of $\mathrm{LP}(\varphi)$ ($\approx 25°$) is larger than that observed between the two PWI stripes in Fig. 3(c): $\Delta\varphi = \varphi_1 - \varphi_0 = 15°$. The shape of the LP becomes compatible with the PWI pattern only if n_{max} is increased, suggesting that a larger number of MHD modes is involved in the PWI than those measured ($n_{max} = 24$) with magnetic sensors.[51] This confirms the clear evidence of modes with $n > 24$, which has already been reported in RFX-mod.[33,52] By taking the analytical expression for LP from Eq. (4), and imposing the distance between the first two minima to be equal to $\Delta\varphi$, one gets

$$n_{max} = 45. \tag{5}$$

The presence of modes with $n > 24$ has already been taken into account for the new design of the magnetic sensors of RFX-mod2,[4,52,53] thus reducing the possibility of large PWI events in the new machine by improving the mode active control, measuring harmonics up to $n_{max} = 36$.

III. ORBIT SIMULATIONS

The analysis of Sec. II is based on the linear superposition of local displacements: it does not take into account the nonlinear interaction of magnetic field lines subject to the whole $m = 0, 1$ spectrum. Therefore, a more refined description of the phenomenon is needed. Here, it is provided via the Hamiltonian guiding center code ORBIT.[46] Tearing modes are given as input to ORBIT in the form: $\delta\vec{B}_{m,n} = \nabla \times \alpha_{m,n}(r)\vec{B}$, where $\alpha_{m,n}(r)$ is a suitable scalar function that contains information about the perturbation with a given (m, n) wavenumber along all the three radial, poloidal, and toroidal directions.[54] The calculation of the perturbation term $\delta\vec{B}_{m,n}$ uses as input the eigenfunctions with $m = 0, 1$ and $n \leq 24$ calculated in toroidal geometry via the NCT code for the same shot (#29324) and time instant ($t = 218$ ms). Then, ORBIT is used to simulate the dynamics of ions with very low energy (10^{-2} eV). Such a low energy has been chosen to accurately describe the magnetic field topology.[55]

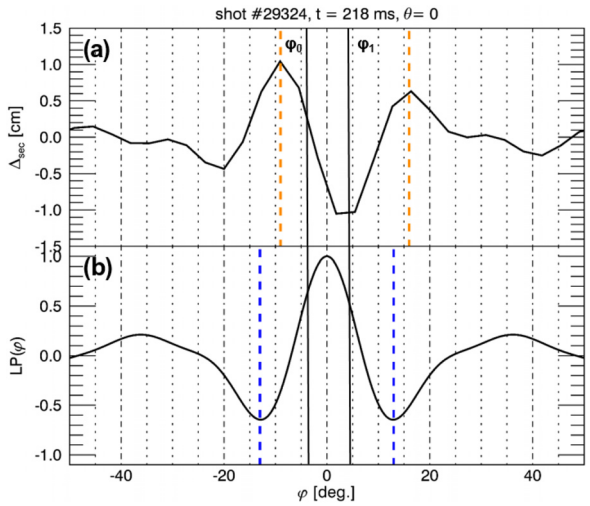

FIG. 4. Comparison between (a) the local displacement of secondary modes, $\Delta_{sec}(\varphi)$, and (b) the locking parameter $\mathrm{LP}(\varphi)$ during shot #29324 at $t = 218$ ms. Dashed orange lines highlight the two maxima of $\Delta_{sec}(\varphi)$, while dashed blue lines indicate the first two minima of $\mathrm{LP}(\varphi)$. The toroidal angles φ_0 and φ_1 of the experimentally observed PWI footprints are highlighted with two solid lines.

A. Poincaré plots

In Fig. 5(a), we report a Poincaré plot considering a large portion of the equatorial plane: $-90° \leq \varphi \leq 90°$, to better observe the PWI region. Each point corresponds to a magnetic field line crossing the plane at $\theta = 0$. Three topologically separated regions are evident: the core region ($0 < r \lesssim 25$ cm) hosts the conserved magnetic islands (pink points) associated with the dominant QSH mode. The presence of this set of islands means that the QSH persists despite the crash, as we expect for a minor event.[20]

The second region ($r > 35$ cm) occupies the plasma edge and it is characterized by a chain of $m = 0$, $n = 7$ islands (cyan and blue points) aligned along the reversal surface (horizontal, green line). Their formation is the main consequence of the toroidal coupling between the $m = 1$, $n = 7$ mode and the Shafranov shift.[49] We notice also that typically a set of smaller $m = 0$ islands surrounds the main $m = 0$, $n = 7$ one. An example of this is shown as blue points in Fig. 5(c) for the $m = 0$ island at $\varphi \approx 130°$. This is a consequence of

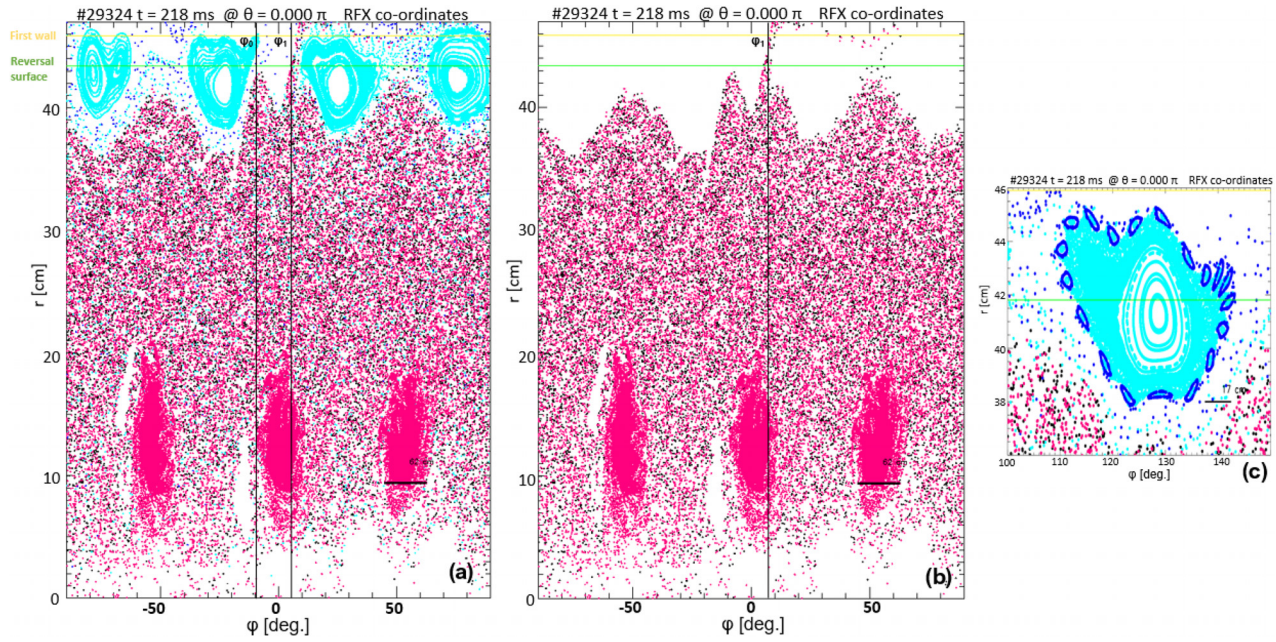

FIG. 5. Toroidal Poincaré plots during the shot #29324 at $t = 218$ ms on the equatorial plane: (a) with full $m = 0, 1$ and $n \leq 24$ spectrum, (b) with $m = 1$ modes, only. Pink points refer to the dominant $m = 1$, $n = 7$ mode. The black points refer to secondary $m = 1$ modes. The cyan points refer to the $m = 0$, $n = 7$ mode. Blue points refer to magnetic field lines due to the resonance of high n, $m = 0$ modes. The horizontal green line represents the reversal surface where $q = 0$, while the yellow line indicates the device first wall. Solid lines represent the toroidal positions, φ_0 and φ_1, of the two PWI footprints experimentally observed. Finally, (c) is a zoomed version in the region near $\varphi \approx 130^\circ$, revealing a Fibonacci sequence of secondary $m = 0$ islands.

the $m = 0$ modes interacting with each other, forming a Fibonacci sequence of smaller islands.[56] The Fibonacci sequence at $\varphi \approx 130^\circ$ is more evident than near $\varphi = 0$, but each $m = 0$ island possesses a chain of secondary islands around its border. The small islands in Fig. 5(c) have $m = 0$, $n = 19$. Since $19 = 7 + 3 \times 4$, we speculate that these could be the first two terms of a sequence of the type $a_{n+1} = a_n + 3 \times a_{n-1}$ with $a_0 = 7$, whose ratio a_n/a_{n+1} converges to $(\sqrt{13} - 1)/6$, i.e., the last Kolmogorov–Arnold–Moser (KAM)[57] conserved surface[58,59] for the $m = 0$ island chain.

Finally, the third region is located between the QSH and the $m = 0$ islands ($25 \lesssim r \lesssim 35$ cm) and it is characterized by a chaotic sea (black and pink points) of magnetic field lines due to the interaction of many secondary ($m = 1$, $n > 7$) modes, which is responsible for magnetic island overlap and chaos.[60] Figure 5(b) is obtained from Fig. 5(a), but removing the $m = 0$ modes from the input to ORBIT. This is done to highlight the convolution of the chaotic sea, which reproduces the profile of the deformation $\Delta_{sec}(\varphi)$ shown in Fig. 4(b). This justifies the use of the local displacement as a first approximation of the magnetic topology. Figure 5(b) clearly shows a bundle of pink and black points protruding from the chaotic sea to the wall at $\varphi \approx 0$, i.e., at the LM location. This means that the PWI stripe located at φ_1 can reasonably be associated with the $m = 1$ Locked Mode. The same argument can be applied also to the second stripe at φ_0. In fact, in Fig. 5(a), there is a smaller set of blue points reaching the wall at φ_0. This suggests that the footprint at φ_0 can be related to ions moving from the tail of the nearest $m = 0$ island to the wall.

B. Calculation of the connection length to the wall and comparison with the experimental PWI image

The Connection Length to the wall $L_{c,w}$ measures the distance along the field line traveled by a ion from a given point $(r^0, \theta^0, \varphi^0)$ to the wall. Formally,

$$L_{c,w}(r^0, \theta^0, \varphi^0) = \int_{\varphi^0}^{\varphi(r_w)} \frac{B\, d\varphi}{\vec{B} \cdot \nabla \varphi}. \tag{6}$$

It is a standard metric used in tokamaks to characterize the ergodic edge when resonant magnetic perturbations (RMPs) are applied.[44,45] In Sec. III A, it has been shown that the RFP edge is characterized by $m = 0$ islands embedded in a chaotic sea,[40,61] and thus it is a suitable environment for the use of this metric. We consider a matrix of initial positions $[r_j^0, \theta_k^0, \varphi_\ell^0]$ with $1 \leq j \leq 8$, $1 \leq k \leq 32$, $1 \leq \ell \leq 64$. Then, to reduce numerical error, $L_{c,w}$ is estimated by averaging over a bundle of 1000 particles, starting at $r^0 = r_j^0$, $\theta^0 = \theta_k^0$ and φ^0 taken from an array of 1000 equally spaced elements centered at φ_ℓ^0. Particles are monoenergetic and collisionless, and energy is the same as in the Poincaré plots.

In Fig. 6(a), we plot the $L_{c,w}(\varphi, r)$ contour together with the Poincaré map in the outermost $\approx$ 10 cm of plasma. The toroidal angle is zoomed in the LM region, with $-40^\circ \leq \varphi \leq 30^\circ$. The Connection Length varies over a wide range between a few centimeters to ten kilometers, which are rather typical values both in the RFP[62] and in the tokamak ergodic divertor.[63] Regions of short $L_{c,w}$ (marked in red in the contour plot) correspond to particle fast losses.[64] In particular, the

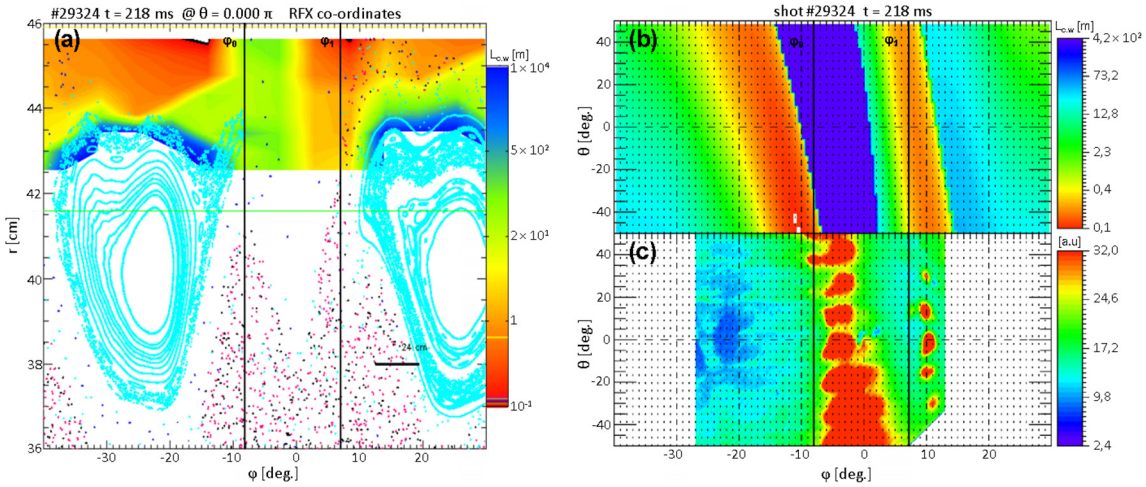

FIG. 6. (a) $L_{c,w}(\varphi, r)$ map and Poincaré plot on a portion of the equatorial plane. Short and long $L_{c,w}$ regions are colored in red and blue, respectively. The toroidal angles φ_0 and φ_1 of the experimentally observed PWI footprints are highlighted with two solid lines. (b) $L_{c,w}(\varphi, \theta)$ map at fixed $r^0 = 45.9$ cm at higher resolution. (c) Image warping of the PWI image in Fig. 3(c). Red regions are those characterized by more intense CI radiation.

toroidal position of the LM at φ_1 is a preferential loss channel that extends deeply in the plasma core, as already shown with ORBIT in the past.[5,33] This result is independent of particle energy, since ORBIT time-steps are normalized to the toroidal transit time. We will anyway discuss in detail the energy dependence in Sec. IV.

In addition to the LM, Fig. 6(a) shows a second region of short $L_{c,w}$ at $\varphi \lesssim \varphi_0$, between the $m = 0$, $n = 7$ island and the wall. This second loss channel is associated with the clockwise rotation of magnetic field lines around the $m = 0$, $n = 7$ island,[40] an additional loss mechanism that has been recently highlighted[61] with the method of Poincaré recurrences.[65] Thus, Fig. 6(a) shows that particles arrive at the wall following two main loss mechanisms: direct parallel loss through the channel at the LM toroidal position φ_1, or clockwise rotation around the $m = 0$, $n = 7$ island closest to the LM, at φ_0.

To better compare with the CCD image, in Fig. 6(b), $L_{c,w}(\varphi, \theta)$ is mapped by keeping fixed the radial coordinate closest to the wall ($r^0 = 45.9$ cm) and varying the angles (θ^0, φ^0) in a grid of 64×128 points in the intervals $-50° \le \theta^0 \le 50°$ and $-40° \le \varphi^0 \le 30°$. The map is compared with the experimental image in Fig. 6(c), obtained by warping Fig. 3(c). A quite good, qualitative agreement between the two images is found. Both theory and experiment show two stripes: a narrower stripe on the right and a wider, more slanted one on the left. However, there are some differences: the stripes in simulation [in Fig. 6(b)] seem to be shifted with respect to the measured angles φ_0 and φ_1 in Fig. 6(c). This can be due to the lack of absolute calibration of the camera alignment with the vacuum vessel.[39] Moreover, the distance between the two stripes is larger than in experiment, but this happens because of the limited number of modes in ORBIT simulations, as extensively explained in Secs. II and III A. Nevertheless, these differences between theory and experiment do not change the main result. The tearing modes determine the pattern of PWI, which is structured in three main regions: the red region of short $L_{c,w}$ to the right corresponds to the PWI stripe at φ_1 associated with the $m = 1$ mode-locking; the second red region on the left is associated with the PWI stripe at φ_0 and is caused by the clockwise rotation around the $m = 0$, $n = 7$ island; finally, the dark blue central region with longer $L_{c,w}$ is associated with the LM counterpart, which does not determine PWI because of the field line pitch, similarly to the unstable manifold in the tokamak homoclinic tangle.[66,67] The result that the $m = 0$, $n = 7$ island causes the larger stripe of CI emission visible in the cameras confirms the important role of $m = 0$ modes in determining the PWI near the LM region, as it was already pointed out in the past in RFX[29] and the Japanese TPE-RX experiment.[68]

C. The 3D nature of connection length

It is common to plot the Connection Length, $L_{c,w}$, as a two-dimensional (2D) map in the (φ, r) or (φ, θ) planes, as it was done in the preceding section following what is customary in tokamaks.[45] The magnetic field in the RFP has anyway an intrinsic three-dimensional (3D) topology, with hidden structures ("streamers" or "cantori") that are not easy to be revealed.[19,64] Now, in this section, we explore the 3D nature of the Connection Length by plotting the maps of $L_{c,w}(\varphi, \theta)$ at inner radii compared to the previous Fig. 6(b).

In Fig. 7, the $L_{c,w}(\varphi, \theta)$ maps are calculated with ORBIT at $r^0 = 45$ cm [Fig. 7(b)] and $r^0 = 44$ cm [Fig. 7(c)]. These maps are compared with the map on the (φ, r) plane shown in Fig. 7(a) with the Poincaré overplotted. The absolute values of $L_{c,w}$ increase overall by moving inward, as expected. At $r = 45$ cm [see Fig. 7(b)], both stripes of short connection lengths are still visible, though shifted toward negative θ angles, which is consistent with the helicity of the LM and the topology of the $m = 0$, $n = 7$ islands.[39] On the contrary, when moving a step inward at $r = 44$ cm, the red stripe associated with the $m = 0$, $n = 7$ island disappears, while the right stripe at φ_1 associated with the LM survives in the contour. This confirms again that the LM corresponds to a channel that delves deeply into the core plasma, as shown in the past in RFX.[5,33] In the place of the left stripe, a set of light-blue filamentary structures of medium $L_{c,w}$ appears. We speculate that these filaments correspond to the secondary $m = 0$ islands in the Fibonacci sequence of smaller islands in the tail of the main 0, 7 island, highlighted with a circle in Fig. 7(a). There is still no direct measurement of these filaments in RFX-mod, but in the future

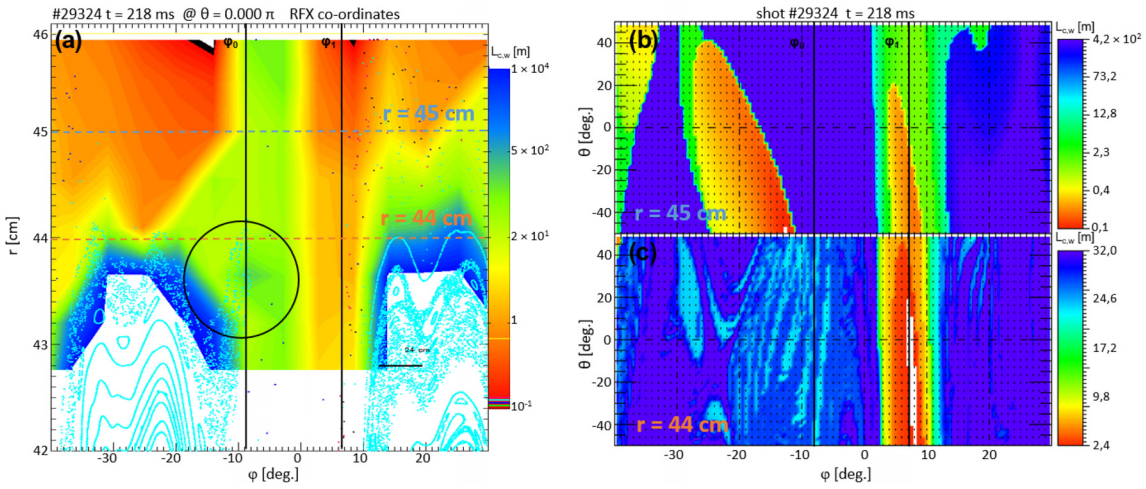

FIG. 7. (a) Zoomed version of the previous Fig. 6(a) near the PWI region. Two horizontal dashed lines represent the radial coordinate corresponding to $r = 45$ cm (in blue) and $r = 44$ cm (in orange). The $m = 0$, $n = 7$ island "tail" is circled. (b) $L_{c,w}(\varphi, \theta)$ map at fixed $r = 45$ cm. (c) $L_{c,w}(\varphi, \theta)$ map at fixed $r = 44$ cm.

RFX-mod2 machine it is foreseen to measure filamentary structures of different nature (high n tearing modes, ELMs, etc.) in both RFP and tokamak configurations, thanks to an unprecedented upgrade of the electrostatic measurement system.[69]

D. Results with an extended MHD spectrum

The analyses of Secs. II and III B show that the experimental PWI image is consistent with $m = 0, 1$ tearing mode spectra with toroidal mode numbers up to $n_{max} = 45$, despite the maximum mode toroidal number of the spectrum that can be experimentally determined in RFX-mod via the pickup coils being $n = 24$, only. It is interesting to repeat ORBIT simulations with a synthetic spectrum of modes, obtained by matching the experimental spectrum for $n \leq 24$ and extrapolating the $\alpha_{m,n}$ functions with $m = 0, 1$ and $24 < n \leq 45$ with a linear decay described by

$$\alpha_{m,n}(r) = \frac{n_{max} + 1 - n}{n_{max} + 1 - n^*} \alpha_{m,n^*}(r), \tag{7}$$

where $n_{max} \equiv 45$ and n^* is a suitable mode near $n = 24$ used for extrapolation. We cannot choose the $n = 24$ mode itself, since this is the last mode in the spectrum and the measurement of its amplitude is polluted, according to the Nyquist theorem. The linear decay in Eq. (7) justifies the weight used for the definition of the LP(φ) function in Eq. (3), and it is shown for $m = 1$ modes in Fig. 8 as a red line.

The eigenfunctions of the extrapolated spectra are shown in Fig. 9. In the case of $m = 1$ modes, the reference mode used for the extrapolation is $n^* = 21$, plotted as a solid, red line in Fig. 9(a): modes with $n > 24$ are obtained from a cubic spline of the $n^* = 21$ up to resonance, see the dashed lines in Fig. 9(a). In the case of $m = 0$ modes, the reference mode used for the extrapolation is $n^* = 22$, again plotted as a solid, red line in Fig. 9(b): modes with $n > 24$ are obtained from a cubic spline of $n^* = 22$ up to the reversal surface [dashed line in Fig. 9(b)]. The reversal surface is in fact the resonance common to all of the $m = 0$ modes. Such a method is similar to that already used in previous works about RFP.[5]

Particular care has been devoted to the choice of the mode phases: our ansatz is that modes with $n > 24$ will maintain the coherence of the Locked Mode. To this extent, mode phases have been chosen considering the following relations:

$$\varphi_{1,n} = n\varphi_{lock} + const, \tag{8}$$

$$\varphi_{0,n} = n\varphi_{lock} - \varphi^*, \tag{9}$$

with $\varphi^* = \pi/2$. The angle φ^* gives reason for the fact that $m = 0$ phase-locking is not exactly symmetric with respect to φ_{lock}, as explained in detail in Ref. 48. Equations (8) and (9) coincide with formulas (13) and (15) of Ref. 48.

In Fig. 10, two images of the Poincaré plot considering modes with $m = 0, 1$ and $0 \leq n \leq 45$ are reported. Figure 10(a) shows the Poincaré plot on the outer half of the equatorial plane. As the former Poincaré plot [Fig. 5(a)] with $n \leq 24$, it is divided into three main

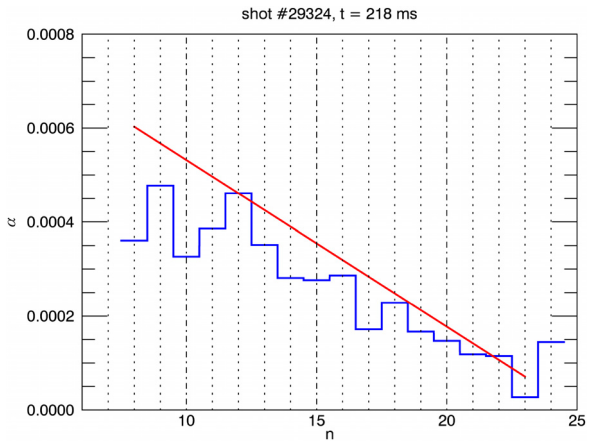

FIG. 8. $m = 1$ secondary mode spectrum during #29324 at $t = 218$ ms. The linear decreasing trend of the $m = 1$ secondary mode amplitudes is highlighted with a red straight line.

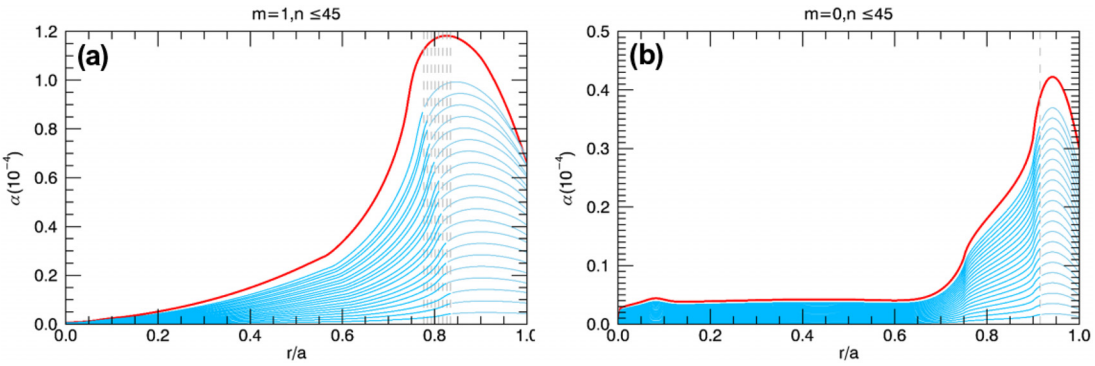

FIG. 9. (a) Extrapolation of the RFX-mod $m = 1$ mode experimental spectrum with toroidal mode numbers $24 < n \leq 45$, Vertical, dashed lines correspond to the resonance surfaces. (b) Same extrapolation for $m = 0$ mode experimental spectrum. The vertical, dashed line corresponds to the reversal surface.

parts: in the inner one there are the dominant $m = 1$, $n = 7$ mode islands (pink points), the mid-radii region is characterized by chaos due to overlap between the $m = 1$ secondary mode islands (black and pink points), while the plasma edge is occupied by the $m = 0$, $n = 7$ islands, which are aligned along the reversal surface (represented as an horizontal green line). As expected, we notice that magnetic chaos is increased with respect to the standard spectrum with $n \leq 24$, as a consequence of the larger number of modes involved. The growth of magnetic chaos is also seen in the Fibonacci sequence of small structures related to secondary $m = 0$ modes around the main islands (blue points) in Fig. 10. These smaller islands are more numerous and distributed more irregularly around the main $m = 0$, $n = 7$ islands.

Another significant consequence of the extended spectrum is that the distance between the two stripes related to the PWI footprints decreases, as expected from the analysis on the Locking Parameter in Sec. II. In Fig. 10(b), we have reported a zoom of the Poincaré plot near the PWI region. The toroidal positions where the points in the Poincaré plot intersect the yellow line representing the first wall are indicated through dashed lines. An excellent agreement with the observed PWI footprint toroidal positions (solid lines), φ_0 and φ_1, is observed. As already seen in Sec. III B, a more quantitative description is obtained by calculating the Connection Length to the wall, taking into account the extended spectrum. In Fig. 11(a), we report the $L_{c,w}(\varphi, \theta)$ map obtained at a fixed radial position ($r^0 = 45.9$ cm) close

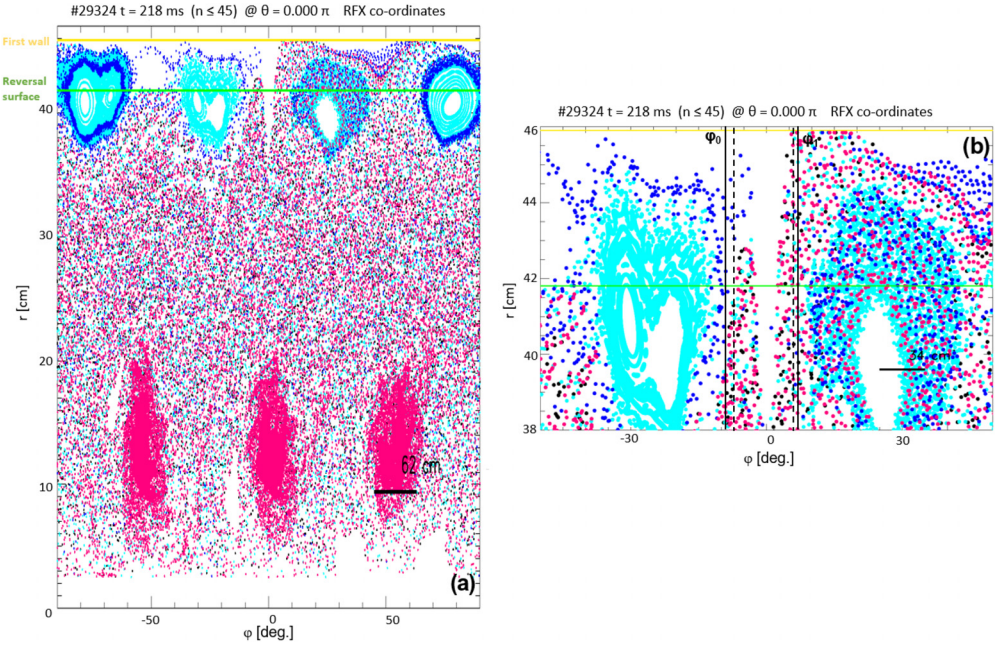

FIG. 10. (a) Toroidal Poincaré plot during the shot #29324 at $t = 218$ ms on the equatorial plane, considering an extended spectrum with modes up to $n = 45$. (b) The same Poincaré plot zoomed in the PWI region. Solid lines represent the toroidal positions, φ_0 and φ_1, of the two PWI footprints experimentally observed. Dashed lines highlight the intersection between the set of points protruding from the chaotic sea, associated with particle losses, and the yellow line representing the device first wall.

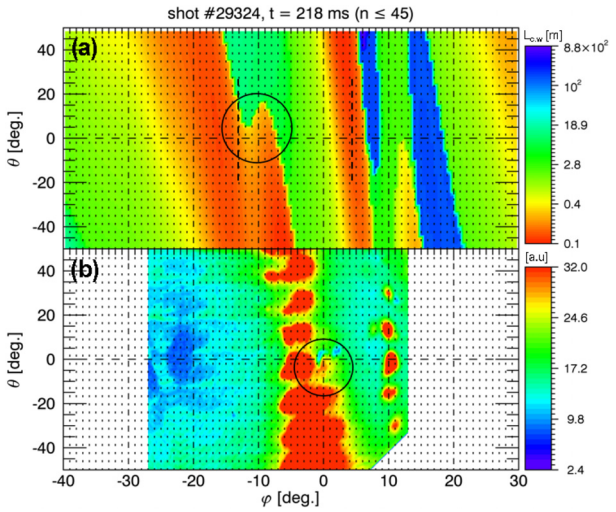

FIG. 11. Comparison between (a) $L_{c,w}(\varphi, \theta)$ map at fixed $r^0 = 45.9$ cm calculated considering an extended spectrum with $0 \leq n \leq 45$, red regions are characterized by short connection lengths, while blue regions are those with long connection lengths; and (b) image warping of the PWI image in Fig. 3(c). Red regions are those characterized by more intense CI radiation. The position of the red stripes is highlighted with dashed lines in the $L_{c,w}$ map. The circles indicate possible corresponding finer structures in the two contours.

to the wall. The map is compared to the warped experimental image of Fig. 3(c). The new map of connection lengths is a significant improvement of the previous one shown in Fig. 6(b): both the distance and the shift between the stripes in Fig. 11(a) are reduced with respect to the measurement in Fig. 11(b). In particular, in the new simulation $\Delta\varphi^{L_{c,w}}_{n_{max}=45} = \varphi^{L_{c,w}}_1 - \varphi^{L_{c,w}}_0 = 18°$, which is coincident (within experimental errors) with the measured distance $\Delta\varphi = 15°$ in the CCD camera image. Actually, with the extended spectrum, the $L_{c,w}$ map reproduces almost exactly, qualitatively and quantitatively, the camera image. Moreover, fine structures appear in the new map, which were absent in the previous Fig. 6(b): see, e.g., the small "bulge" on the right side of the m = 0 stripe, highlighted with a circle in Fig. 11(a). This can be likely associated with a small structure that is present also in the experimental image, located almost in the same position in the φ–θ plane and indicated with a circle in Fig. 11(b). We speculate that this "bulge" can be due to secondary Fibonacci islands around the main 0,7 island placed immediately to the left of the LM.

IV. ORBIT RUNS WITH ENERGETIC IONS

In the preceding sections, ORBIT simulations are performed with low-energy ions (field lines), but to assess the impact of the topological structures on the measured PWI, higher particle energy is required. To do this, we use the same matrix of initial positions $[r^0_j, \theta^0_k, \varphi^0_\ell]$ as in Fig. 7(c) with $r^0 = 44$ cm and a grid of 64×128 points in the intervals $-50° \leq \theta^0 \leq 50°$ and $-40° \leq \varphi^0 \leq 30°$. Now, instead of monoenergetic, cold ions (field lines), each run is launched considering a Maxwellian population of 1000 ions with initial temperature $T_0 = 402$ eV and a tail up to $E = 2$ keV. In the calculation, we put as initial temperature $T_0 = T_e$, with T_e the electron temperature measured at $t = 218$ ms. This assumption is based on measurements on the MST reversed-field pinch, and it is a reasonable condition during a crash.[70] Ions are allowed to collide with the background (electrons and ions) and are deposited with random pitch λ with the corresponding initial positions in the matrix. Collisions are implemented in ORBIT with a simple Monte Carlo energy conserving, pitch angle scattering operator, based on the Boozer–Kuo approach.[71] Since each particle now has a different energy, we cannot use $L_{c,w}$ as a metric: instead, we use the loss time τ_{loss}, defined as the time spent by 50% plus one ions to reach the wall.[5] Figure 12 shows the comparison between the new τ_{loss} map and the $L_{c,w}(\varphi, \theta)$ map of Fig. 6(b), here reported for convenience in panel (a). τ_{loss} varies from 1 ms to about 80 ms. As somewhat expected, energetic ions are lost in a very short time, $\tau_{loss} \approx 1$ ms, at the LM toroidal position [red stripe on the right in Fig. 12(b)]. This result confirms the importance of the LM in determining the PWI, which was found in the past years on RFX both experimentally[28–33] and in simulations.[5] On the contrary, the $m = 0$ footprint is still visible as a fainter stripe on the left of Fig. 12(b), but it is associated with longer loss times, $\tau_{loss} \approx 10$ ms.

Finally, running energetic ions, it is also possible to look at the energy and pitch histograms of particles lost near the Locked Mode and near the $m = 0$ island. This is illustrated in Fig. 13: we sample a few runs related to the $m = 0$ island and the LM, respectively, and marked with crosses (+) in Fig. 12(b): the energy and pitch (λ) histograms relative to the LM are shown in Figs. 13(a) and 13(b), while the same histograms for the $m = 0$ island are shown in Figs. 13(c) and 13(d).

From Figs. 13(a) and 13(b), it follows that counter-passing fast ions with $E > T_0$ are the most important component in the PWI near the Locked Mode, and they are quickly lost. In fact, the average energy (temperature) of ions lost near the LM is $T_{\text{lost}} = 424$ eV $> T_0 = 402$eV. This is reasonable, since the connection length is a property of the magnetic field that does not depend on particle energy: it follows that superthermal ions, which are also less collisional than thermal

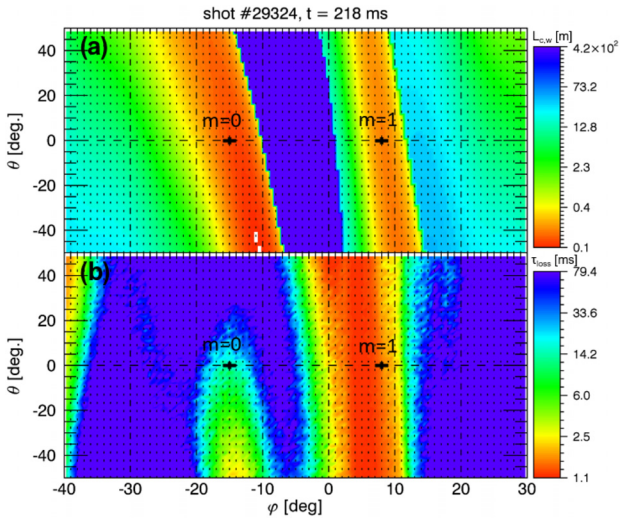

FIG. 12. Comparison between (a) $L_{c,w}(\varphi, \theta)$ map at fixed radius: $r = 45.9$ cm calculated using monoenergetic cold ions, and (b) $\tau_{loss}(\varphi, \theta)$ at fixed radius: $r = 44$ cm, calculated using Maxwellian ions with $T = 402$ eV. To the left, there is the $m = 0$ island loss channel. To the right, there is the $m = 1$ LM loss channel. Crosses (+) indicate the runs that are considered for the statistics of energy and pitch in Fig. 13.

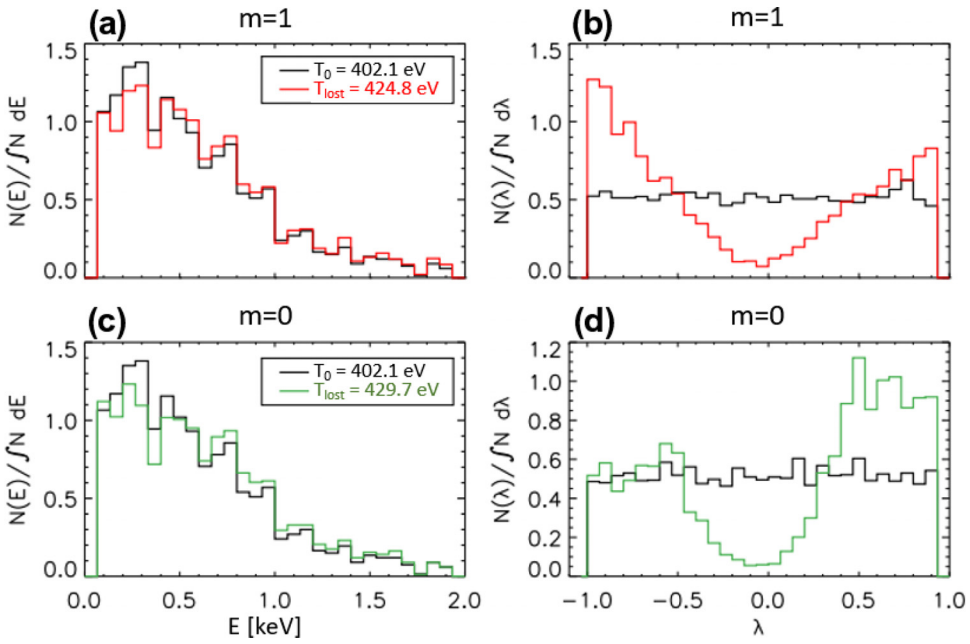

FIG. 13. (a)–(c) Energy and (b)–(d) pitch histograms: (a)–(b) are related to the LM channel, while (c)–(d) are related to the $m = 0$ island. The initial Maxwell distribution with $T_0 = 402$ eV is shown in black and the final distribution are shown in color. The initial pitch distribution is flat (random values in $[-1, 1]$).

ones, are quickly lost. This is also the physical reason why the LM is such an efficient loss channel of hot particles coming directly from the core plasma: ions remaining in the simulation cool down at $T_i = 379$ eV in only 1 ms, which is similar to the fast cooling down process observed experimentally, e.g., in Fig. 2(d). This mechanism may also explain the "anomalous" component in the Spitzer resistivity appearing in the RFP and which seems to be a general issue with plasma collisionless regimes.[72] Regarding the pitch in Fig. 13(b), it is noteworthy that trapped particles are not involved in the loss mechanism: magnetic chaos does not act on them, as it was already found in ORBIT simulations on RFX.[64,73,74]

In the $m = 0$ island region [see Figs. 13(c) and 13(d)], the loss mechanism is pretty similar to the LM: in this case, co-passing, fast ions are the main loss channel, with $T_{\text{lost}} = 429$ eV $> T_0 = 402$ eV, and remaining ions cooling down to $T_i = 374$ eV. Nevertheless, since the $m = 0$ loss time is longer [see Fig. 12(b)], it follows that the power lost is smaller by a factor 10. In this sense, the $m = 0$ island chain acts similarly to the "island divertor" in stellarators, spreading the energy losses on a larger area and on longer times.[63] The possibility of exploiting the $m = 0$ islands as a naturally occurring divertor in the RFP was already pointed out in the past.[75] This is important also as a perspective for the upgraded RFX-mod2 device, since, by reducing the Locked Mode deformation, we expect to reduce also the PWI.[76]

V. CONCLUSIONS

In this paper, we have studied the magnetic topology during a reconnection event in the RFX-mod reversed-field pinch. We have shown that, during the crash, the increase in amplitude of the $m = 1$ tearing modes with $n > 7$, together with their phase-locking, determines transient and localized particle losses, and consequent strong plasma–wall interaction (PWI). Through a linear study of the LCFS displacement, we have shown that modes with very high n, up to $n_{max} = 45$, are involved in the PWI event. A more refined analysis of the chaotic magnetic field topology, and field line connection lengths, with the code ORBIT shows that the camera images of the PWI pattern are consistent with the map of connection lengths near the wall. In particular, to reproduce with high precision the PWI pattern experimentally observed, it is necessary to include in simulations an extended spectrum with $m = 0, 1$ and $0 < n \leq 45$, meaning that high n modes ($n > 24$) are important, despite their low amplitude. Moreover, filamentary structures with $m = 0$ and medium n ($n = 13 \sim 19$) located more deeply in the plasma edge are seen in the 3D maps of connection lengths. These filaments have not yet been measured, but it is foreseen to do that with an improved electrostatic sensor array in the future RFX-mod2 device, which should be commissioned starting from the end of 2024.

Moreover, in the future RFX-mod2, an upgrade of magnetic pickup arrays will allow for overcoming the limitation in toroidal resolution to $n \leq 24$, bringing improved measurements (up to $n_{max} = 36$) and simulations. At the same time, this will allow for better feedback control of tearing modes in order to mitigate/avoid major crashes and their associated loss of confinement. Finally, an improved optical camera system (OCS) of 7 fast cameras covering a large part (around 70%) of the wall will be installed, allowing for better spatial characterization of observable PWI phenomena as well as increasing the number of observations of such events.

Runs with a Maxwellian population of particles show that the Locked Mode is a very efficient loss channel of counter-passing, fast ions: conserved ions are subject to a very rapid cooling process, ≈ 10 eV in only 1 ms. This process is similar for the $m = 0$ island, but the loss times are much longer, $\tau_{loss} \approx 10$ ms, and the associated PWI is a factor 10 smaller. We conclude that the $m = 0$ island chain acts similarly to the "island divertor" in stellarators, spreading the energy losses on a larger area and on longer times.[63] This is a good perspective

for the upgraded RFX-mod2 device, since, by reducing the Locked Mode deformation, we expect to reduce also the PWI.[76]

ACKNOWLEDGMENTS

This work has been carried out within the framework of the Italian National Recovery and Resilience Plan (NRRP), funded by the European Union - NextGenerationEU (Mission 4, Component 2, Investment 3.1 - Area ESFRI Energy - Call for tender No. 3264 of 28–12–2021 of Italian University and Research Ministry (MUR), Project ID IR0000007, MUR Concession Decree No. 243 del 04/08/2022, CUP B53C22003070006, "NEFERTARI – New Equipment for Fusion Experimental Research and Technological Advancements with Rfx Infrastructure"). Views and opinions expressed are however those of the author(s) only and do not necessarily reflect those of the European Union or the European Commission. Neither the European Union nor the European Commission can be held responsible for them. The authors wish to thank Maria Ester Puiatti, Paolo Scarin, Lorella Carraro, Lionello Marrelli, and Paolo Zanca for useful suggestions and fruitful discussions.

AUTHOR DECLARATIONS

Conflict of Interest

The authors have no conflicts to disclose.

Author Contributions

P. Porcu: Conceptualization (equal); Data curation (equal); Formal analysis (equal); Methodology (equal); Software (equal); Validation (equal); Writing – original draft (equal); Writing – review & editing (equal). **G. Spizzo:** Conceptualization (equal); Funding acquisition (equal); Methodology (equal); Software (equal); Supervision (equal); Validation (equal); Writing – original draft (equal); Writing – review & editing (equal). **M. Veranda:** Conceptualization (equal); Formal analysis (equal); Methodology (equal); Writing – review & editing (equal). **M. Zuin:** Conceptualization (equal); Funding acquisition (equal); Supervision (equal); Writing – review & editing (equal). **M. Agostini:** Conceptualization (equal); Data curation (equal); Validation (equal); Writing – review & editing (equal). **M. Gobbin:** Data curation (equal); Methodology (equal); Software (equal); Validation (equal). **D. Terranova:** Conceptualization (equal); Data curation (equal); Methodology (equal); Software (equal); Validation (equal); Writing – review & editing (equal).

DATA AVAILABILITY

The data that support the findings of this study are available from the corresponding author upon reasonable request.

APPENDIX: CALCULATION OF THE LOCKING PARAMETER AS A FUNCTION OF THE NUMBER OF MODES

In this section, we clarify the main passages of the calculation leading from Eq. (3) to the analytic version of the Locking Parameter LP reported in Eq. (4). Moreover, we discuss the derivation of the maximum toroidal number (5) of the locked modes causing the PWI of interest in this work.

The starting expression for LP was

$$\mathrm{LP}(\varphi) = \frac{2}{(n_{max}-6)(n_{max}-7)} \sum_{\ell=8}^{n_{max}} (n_{max}+1-\ell)\cos(n\varphi). \quad \text{(A1)}$$

First, we decided to compare the toroidal profile of LP just obtained, calculated with $n_{max} = 23$, with the displacement one, which takes into account the same spectrum: $m = 1$, $8 \le n \le 23$. This comparison is shown in Fig. 4 and looks optimal. In fact, measuring the distance between the two maxima of the local displacements, we get: $\Delta\varphi^{\Delta} = 25°$, while the distance between the two minima of the $\mathrm{LP}(\varphi)$ is $\Delta\varphi^{\mathrm{LP}}_{n_{max}=23} = 26°$.

For brevity, in the rest of this section we will rename the variable: $n_{max} \to N$.

In Eq. (5), we estimated the maximum toroidal number of the modes involved in the LM, by imposing that the distance between the two LP minima (whose profile depends on the choice of n_{max}) is that experimentally measured: $\Delta\varphi = 15°$. Therefore, we needed to recast an analytical version for (A1) in order to calculate its first derivative,

$$\begin{aligned}\mathrm{LP}(\varphi) &= \frac{2}{(N-6)(N-7)} \\ &\quad \times \left[\sum_{\ell=1}^{N}(N+1-\ell)\cos(\ell\varphi) - \sum_{\ell=1}^{7}(N+1-\ell)\cos(\ell\varphi)\right] \\ &= \mathrm{LP}^*(\varphi) - \frac{2\,A_N(\varphi)}{(N-6)(N-7)}, \end{aligned} \quad \text{(A2)}$$

where $A_N(\varphi) = \sum_{\ell=1}^{7}(N+1-\ell)\cos(\ell\varphi)$. The quantity LP^* is defined by

$$\begin{aligned}\mathrm{LP}^*(\varphi) &= \frac{2(N+1)}{(N-6)(N-7)} \\ &\quad \times \sum_{\ell=1}^{N}\cos(\ell\varphi) - \frac{2}{(N-6)(N-7)}\sum_{\ell=1}^{n}\ell\cos(\ell\varphi) \\ &= \frac{(N+1)}{(N-6)(N-7)}\left[\frac{1}{\sin\left(\frac{\varphi}{2}\right)}\sin\left[\left(N+\frac{1}{2}\right)\varphi\right] - 1\right] \\ &\quad - \frac{1}{2(N-6)(N-7)\sin^2\left(\frac{\varphi}{2}\right)} \\ &\quad \times \{(N+1)\cos(N\varphi) - N\cos[(N+1)\varphi] - 1\}. \end{aligned} \quad \text{(A3)}$$

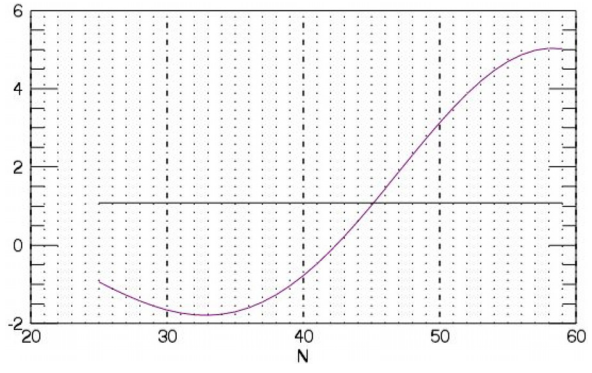

FIG. 14. Graphical solution of Eq. (A5). The equation's left-hand side trend is shown in purple, while the right-hand side trend is shown in black.

$\mathrm{LP}(\varphi)$ is an even function, so the distance $\Delta\varphi^{\mathrm{LP}}$ between its minima can be written as $\Delta\varphi = 2\hat{\varphi}$ where $\hat{\varphi}$ is the position of the minimum with $\hat{\varphi} > 0$. The first derivative of $\mathrm{LP}(\varphi)$ in Eq. (A3) is

$$\begin{aligned}\frac{\mathrm{dLP}}{\mathrm{d}\varphi} = &\frac{1}{2(N-6)(N-7)}\frac{1}{\sin^3\left(\frac{\varphi}{2}\right)}\\ &\times\left\{2(N+1)\left(N+\frac{1}{2}\right)\sin^2\left(\frac{\varphi}{2}\right)\cos\left[\left(N+\frac{1}{2}\right)\varphi\right]\right.\\ &-(N+1)\sin\left(\frac{\varphi}{2}\right)\cos\left(\frac{\varphi}{2}\right)\sin\left[\left(N+\frac{1}{2}\right)\varphi\right]\\ &-N(N+1)\sin\left(\frac{\varphi}{2}\right)\sin[(N+1)\varphi]\\ &+N(N+1)\sin\left(\frac{\varphi}{2}\right)\sin(N\varphi)\\ &+\cos\left(\frac{\varphi}{2}\right)\{(N+1)\cos(N\varphi)-N\cos[(N+1)\varphi]-1\}\\ &\left.+4(N+1)B(\varphi)\sin^3\frac{\varphi}{2}-4C(\varphi)\sin^3\frac{\varphi}{2}\right\},\end{aligned} \tag{A4}$$

where $B(\varphi)$ and $C(\varphi)$ are, respectively, given by

$$\begin{aligned}B(\varphi) &= \sum_{\ell=1}^{7}\ell\sin(\ell\varphi),\\ C(\varphi) &= \sum_{\ell=1}^{7}\ell^2\sin(\ell\varphi).\end{aligned}$$

By imposing that the condition of minimum $\left(\frac{\mathrm{dLP}}{\mathrm{d}\varphi}(\varphi_S) = 0\right)$ is satisfied for the experimentally measured position of the PWI stripe ($\varphi_S = 7.5°$), one gets the following equation to be solved in the variable N:

$$\begin{aligned}&\left[2N\sin^2\left(\frac{\varphi_S}{2}\right)+1\right]\cos\left[\left(N+\frac{1}{2}\right)\varphi_S\right]\\ &\quad+N\sin\left(\frac{\varphi_S}{2}\right)\left[\sin(N\varphi_S)+4\sin^2\left(\frac{\varphi_S}{2}\right)B(\varphi_S)\right]\\ &\quad=\cos\left(\frac{\varphi_S}{2}\right)-4\sin^3\left(\frac{\varphi_S}{2}\right)[B(\varphi_S)-C(\varphi_S)].\end{aligned} \tag{A5}$$

Then, we solved this equation graphically, as shown in Fig. 14. We obtain

$$N = 45. \tag{A6}$$

REFERENCES

[1]S. Ortolani and the RFX Team, "Active MHD control experiments in RFX-mod," Plasma Phys. Controlled Fusion **48**, B371 (2006).
[2]G. Rostagni, "RFX: An expected step in RFP research," Fusion Eng. Des. **25**, 301 (1995).
[3]L. Marrelli, P. Martin, M. Puiatti, J. Sarff, B. Chapman, J. Drake, D. Escande, and S. Masamune, "The reversed field pinch," Nucl. Fusion **61**, 023001 (2021).
[4]L. Marrelli, R. Cavazzana, D. Bonfiglio, M. Gobbin, G. Marchiori, S. Peruzzo, M. Puiatti, G. Spizzo, D. Voltolina, P. Zanca, M. Zuin, G. Berton, P. Bettini, T. Bolzonella, A. Canton, S. Cappello, L. Carraro, L. Cordaro, S. D. Bello, M. D. Palma, G. D. Masi, A. Fassina, F. Gnesotto, L. Grando, P. Innocente, F. Lunardon, G. Manduchi, D. Marcuzzi, N. Marconato, R. Piovan, N. Pomaro, A. Rigoni, A. Rizzolo, P. Scarin, M. Siragusa, P. Sonato, S. Spagnolo, M. Spolaore, D. Terranova, and the RFX-mod Team, "Upgrades of the RFX-mod reversed field pinch and expected scenario improvements," Nucl. Fusion **59**, 076027 (2019).
[5]G. Spizzo, S. Cappello, A. Cravotta, D. F. Escande, I. Predebon, L. Marrelli, P. Martin, and R. B. White, "Transport barrier inside the reversal surface in the chaotic regime of the reversed-field pinch," Phys. Rev. Lett. **96**, 025001 (2006).
[6]M. Gobbin, P. Franz, R. Lorenzini, I. Predebon, A. Ruzzon, A. Fassina, L. Marrelli, B. Momo, and D. Terranova, "Heat transport in helical RFX-mod plasmas by electron temperature dynamics from soft-x-ray diagnostics," Plasma Phys. Controlled Fusion **55**, 105010 (2013).
[7]S. Cappello and D. Biskamp, "Reconnection processes and scaling laws in reversed field pinch magnetohydrodynamics," Nucl. Fusion **36**, 571 (1996).
[8]P. Martin, L. Marrelli, G. Spizzo, P. Franz, P. Piovesan, I. Predebon, T. Bolzonella, S. Cappello, A. Cravotta, D. Escande, L. Frassinetti, S. Ortolani, R. Paccagnella, D. Terranova, B. Chapman, D. Craig, S. Prager, J. Sarff, t M. team, P. Brunsell, J.-A. Malmberg, J. Drake, t E. T. team, Y. Yagi, H. Koguchi, Y. Hirano, R. White, C. Sovinec, C. Xiao, R. Nebel, D. Schnack, and the TPE-RX Team. the RFX Team, "Overview of quasi-single helicity experiments in reversed field pinches," Nucl. Fusion **43**, 1855 (2003).
[9]R. Lorenzini, E. Martines, P. Piovesan, D. Terranova, P. Zanca, M. Zuin, A. Alfier, D. Bonfiglio, F. Bonomo, A. Canton, S. Cappello, L. Carraro, R. Cavazzana, D. F. Escande, A. Fassina, P. Franz, M. Gobbin, P. Innocente, L. Marrelli, R. Pasqualotto, M. E. Puiatti, M. Spolaore, M. Valisa, N. Vianello, P. Martin, and RFX-mod Team and collaborators, "Self-organized helical equilibria as a new paradigm for ohmically heated fusion plasmas," Nat. Phys. **5**, 570 (2009).
[10]W. F. Bergerson, F. Auriemma, B. E. Chapman, W. X. Ding, P. Zanca, D. L. Brower, P. Innocente, L. Lin, R. Lorenzini, E. Martines, B. Momo, J. S. Sarff, and D. Terranova, "Bifurcation to 3D helical magnetic equilibrium in an axisymmetric toroidal device," Phys. Rev. Lett. **107**, 255001 (2011).
[11]L. Frassinetti, I. Predebon, H. Koguchi, Y. Yagi, Y. Hirano, H. Sakakita, G. Spizzo, and R. B. White, "Improved particle confinement in transition from multiple-helicity to quasi-single-helicity regimes of a reversed-field pinch," Phys. Rev. Lett. **97**, 175001 (2006a).
[12]L. Frassinetti, P. R. Brunsell, J. R. Drake, S. Menmuir, and M. Cecconello, "Spontaneous quasi single helicity regimes in EXTRAP T2R reversed-field pinch," Phys. Plasmas **14**, 112510 (2007).
[13]K. Oki, D. Fukahori, K. Deguchi, S. Nakaki, A. Sanpei, H. Himura, S. Masamune, and R. Paccagnella, "Characterization of quasi-single-helicity states in a low-aspect-ratio RFP," Plasma Fusion Res. **7**, 1402028 (2012).
[14]J. B. Taylor, "Relaxation of toroidal plasma and generation of reverse magnetic fields," Phys. Rev. Lett. **33**, 1139 (1974).
[15]S. Cappello, D. Bonfiglio, D. F. Escande, S. C. Guo, A. Alfier, R. Lorenzini, and the RFX Team, "The reversed field pinch toward magnetic order: A genuine self-organization," AIP Conf. Proc. **1069**, 27 (2008).
[16]Y. L. Ho, D. D. Schnack, P. Nordlund, S. Mazur, H. Satherblom, J. Scheffel, and J. R. Drake, "Effect of aspect ratio on magnetic field fluctuations in the reversed-field pinch," Phys. Plasmas **2**, 3407 (1995).
[17]T. Bolzonella and D. Terranova, "Magnetic fluctuation spectra and non-linear MHD mode interaction in RFX," Plasma Phys. Controlled Fusion **44**, 2569 (2002).
[18]P. Piovesan, M. Zuin, A. Alfier, D. Bonfiglio, F. Bonomo, A. Canton, S. Cappello, L. Carraro, R. Cavazzana, D. Escande, A. Fassina, M. Gobbin, R. Lorenzini, L. Marrelli, P. Martin, E. Martines, R. Pasqualotto, M. Puiatti, M. Spolaore, M. Valisa, N. Vianello, P. Zanca, R. F. X. the, and T. mod, "Magnetic order and confinement improvement in high-current regimes of RFX-mod with MHD feedback control," Nucl. Fusion **49**, 085036 (2009).
[19]M. Veranda, D. Bonfiglio, S. Cappello, G. di Giannatale, and D. F. Escande, "Helically self-organized pinches: Dynamical regimes and magnetic chaos healing," Nucl. Fusion **60**, 016007 (2020).
[20]M. Gobbin, M. Agostini, F. Auriemma, L. Carraro, R. Cavazzana, A. Fassina, P. Franz, L. Marrelli, B. Momo, R. Piovan, I. Predebon, M. Puiatti, G. Spizzo, D. Terranova, M. Zuin, and the RFX-mod Team, "Ion heating and energy balance

during magnetic reconnection events in the RFX-mod experiment," Nucl. Fusion **62**, 026030 (2022).
[21]B. Momo, H. Isliker, R. Cavazzana, M. Zuin, L. Cordaro, D. Lopez-Bruna, E. Martines, I. Predebon, C. Rea, M. Spolaore, L. Vlahos, and P. Zanca, "The phenomenology of reconnection events in the reversed field pinch," Nucl. Fusion **60**, 056023 (2020).
[22]M. Veranda, S. Cappello, D. Bonfiglio, F. D. Escande, and A. Kryzhanovskyy, "Magnetic reconnection in three-dimensional quasi-helical pinches," Rendiconti Lincei. Scienze Fisiche e Naturali **31**, 963 (2020).
[23]V. Antoni and S. Ortolani, "Relaxation phenomena and on axis q limit in a reversed field pinch," Phys. Fluids **30**, 1489 (1987).
[24]S. C. Prager, "Dynamo and anomalous transport in the reversed field pinch," Plasma Phys. Controlled Fusion **41**, A129 (1999).
[25]M. Gobbin, D. Bonfiglio, D. F. Escande, A. Fassina, L. Marrelli, A. Alfier, E. Martines, B. Momo, and D. Terranova, "Vanishing magnetic shear and electron transport barriers in the RFX-mod reversed field pinch," Phys. Rev. Lett. **106**, 025001 (2011).
[26]T. Tamano, W. D. Bard, C. Chu, Y. Kondoh, R. J. La Haye, P. S. Lee, M. Saito, M. J. Schaffer, and P. L. Taylor, "Observation of a new toroidally localized kink mode and its role in reverse-field-pinch plasmas," Phys. Rev. Lett. **59**, 1444 (1987).
[27]K. Kusano, T. Tamano, and T. Sato, "MHD simulation of the toroidal phase locking mechanism in a reversed field pinch plasma," Nucl. Fusion **31**, 1923 (1991).
[28]V. Antoni, M. Bagatin, H. Bergsåker, G. Della Mea, D. Desideri, E. Martines, V. Rigato, G. Serianni, P. Sonato, L. Tramontin, and S. Zandolin, "Plasma wall interaction and energy fluxes in RFX," J. Nucl. Mater. **220–222**, 650 (1995).
[29]P. Zanca, D. Bettella, S. Martini, and M. Valisa, "Non-axisymmetric perturbation of the plasma surface in RFX: Analysis of magnetic data versus CCD images of plasma-wall interaction," J. Nucl. Mater. **290–293**, 990 (2001a).
[30]P. Zanca, D. Terranova, M. Valisa, and S. Dal Bello, "Plasma wall interactions in RFX-mod with virtual magnetic boundary," J. Nucl. Mater. **363–365**, 733 (2007).
[31]M. Valisa, T. Bolzonella, L. Carraro, E. Casarotto, S. Costa, L. Garzotti, P. Innocente, S. Martini, R. Pasqualotto, M. Puiatti, R. Pugno, and P. Scarin, "Locked modes induced plasma-wall interactions in RFX," J. Nucl. Mater. **241–243**, 988 (1997).
[32]L. Marrelli, P. Zanca, P. Martin, S. Martini, and A. Munari, "Edge localised asymmetric radiative phenomena in RFX," J. Nucl. Mater. **266–269**, 877 (1999).
[33]P. Scarin, M. Agostini, G. Spizzo, M. Veranda, P. Zanca, and the RFX-mod Team, "Helical plasma-wall interaction in the RFX-mod: Effects of high-n mode locking," Nucl. Fusion **59**, 086008 (2019).
[34]R. Pasqualotto, R. Pugno, M. Valisa, L. Carraro, M. Puiatti, F. Sattin, and P. Scarin, "The CCD camera based imaging system on RFX," Plasma Devices Oper. **5**, 287 (1998).
[35]P. Zaccaria, S. Dal Bello, and D. Marcuzzi, "Tests and analyses for the mechanical and thermal qualification of the new RFX first wall tiles," Fusion Eng. Des. **66–68**, 289 (2003).
[36]L. Frassinetti, Y. Yagi, H. Koguchi, T. Shimada, Y. Hirano, and H. Sakakita, "Toroidally localized soft x-ray expulsion at the termination of the improved confinement regime in the TPE-RX reversed-field pinch experiment," Phys. Plasmas **13**, 042502 (2006b).
[37]P. Zanca, "Avoidance of tearing modes wall-locking in a reversed field pinch with active feedback coils," Plasma Phys. Controlled Fusion **51**, 015006 (2009).
[38]M. Agostini, A. Scaggion, P. Scarin, G. Spizzo, and N. Vianello, "Interplay between edge magnetic topology, pressure profile and blobs in the edge of RFX-mod," Plasma Phys. Controlled Fusion **54**, 065003 (2012).
[39]M. Agostini, P. Scarin, G. Spizzo, F. Auriemma, S. Cappello, L. Carraro, L. Marrelli, S. Spagnolo, M. Spolaore, M. Veranda, N. Vianello, M. Zuin, and the RFX-mod Team, "Edge plasma properties with 3D magnetic perturbations in RFX-mod," Nucl. Fusion **57**, 076033 (2017).
[40]G. Spizzo, M. Agostini, P. Scarin, R. White, O. Schmitz, M. Spolaore, D. Terranova, M. Veranda, and N. Vianello, "Toroidal coupling in the kinetic response to edge magnetic perturbations," Nucl. Fusion **57**, 126055 (2017).
[41]A. Gude, M. Maraschek, V. Igochine, B. Sieglin, M. Willensdorfer, and H. Zohm, "Phase relation between rotating phase locked (2, 1) and (3, 1) tearing modes in ASDEX Upgrade," Plasma Phys. Controlled Fusion **63**, 045018 (2021).
[42]V. Igochine, O. Dumbrajs, D. Constantinescu, H. Zohm, G. Zvejnieks, and the ASDEX Upgrade Team, "Stochastization as a possible cause for fast reconnection during MHD mode activity in the ASDEX Upgrade tokamak," Nucl. Fusion **46**, 741 (2006).
[43]P. de Vries, G. Pautasso, E. Nardon, P. Cahyna, S. Gerasimov, J. Havlicek, T. Hender, G. Huijsmans, M. Lehnen, M. Maraschek, T. Markovič, J. Snipes, and the COMPASS Team, the ASDEX Upgrade Team, and JET Contributors, "Scaling of the MHD perturbation amplitude required to trigger a disruption and predictions for ITER," Nucl. Fusion **56**, 026007 (2016).
[44]F. Nguyen, P. Chendrih, and A. Grosman, "Interaction of stochastic boundary layer with plasma facing components," Nucl. Fusion **37**, 743 (1997).
[45]O. Schmitz, M. Jakubowski, H. Frerichs, D. Harting, M. Lehnen, B. Unterberg, S. Abduallaev, S. Brezinsek, I. Classen, T. Evans, Y. Feng, K. Finken, M. Kantor, D. Reiter, U. Samm, B. Schweer, G. Sergienko, G. Spakman, M. Tokar, E. Uzgel, R. Wolf, and T. the TEXTOR, "Identification and analysis of transport domains in the stochastic boundary of TEXTOR-DED for different mode spectra," Nucl. Fusion **48**, 024009 (2008).
[46]R. B. White and M. S. Chance, "Hamiltonian guiding center drift orbit calculation for plasmas of arbitrary cross section," Phys. Fluids **27**, 2455 (1984).
[47]H. Zohm, *Magnetohydrodynamic Stability of Tokamaks* (Wiley-VCH Verlag GmbH & Co. KGaA, 2014), Chap. 8.2, pp. 127–134.
[48]P. Zanca, E. Martines, T. Bolzonella, S. Cappello, S. C. Guo, P. Martin, S. Martini, S. Ortolani, R. Paccagnella, D. Terranova, and M. Viterbo, "Analysis of phase locking of tearing modes in reversed field pinch plasmas," Phys. Plasmas **8**, 516 (2001b).
[49]P. Zanca and D. Terranova, "Reconstruction of the magnetic perturbation in a toroidal reversed field pinch," Plasma Phys. Controlled Fusion **46**, 1115 (2004).
[50]P. Fitzpatrick and P. Zanca, "Phase-locking of tearing modes in the reversed field experiment," Phys. Plasmas **9**, 2707 (2002).
[51]P. Fiorentin and N. Pomaro, "Design of a new electromagnetic diagnostic for RFX," Fusion Eng. Des. **66–68**, 871 (2003).
[52]G. Marchiori, R. Cavazzana, P. Bettini, L. Grando, and S. Peruzzo, "Upgraded electromagnetic measurement system for RFX-mod," Fusion Eng. Des. **123**, 892 (2017).
[53]N. Marconato, P. Bettini, R. Cavazzana, L. Grando, G. Marchiori, L. Marrelli, S. Peruzzo, and N. Pomaro, "Design of the new electromagnetic measurement system for RFX-mod upgrade," Fusion Eng. Des. **146**, 906 (2019).
[54]R. B. White, "Representation of ideal magnetohydrodynamic modes," Phys. Plasmas **20**, 022105 (2013).
[55]G. Ciaccio, M. Veranda, D. Bonfiglio, S. Cappello, G. Spizzo, L. Chacón, and R. B. White, "Numerical verification of orbit and nemato codes for magnetic topology diagnosis," Phys. Plasmas **20**, 062505 (2013).
[56]R. B. White, *The Theory of Toroidally Confined Plasmas*, 3rd ed. (Imperial College Press, London, 2014), Chap. 6.4, pp. 236–238.
[57]A. J. Lichtenberg and M. A. Lieberman, *Regular and Chaotic Dynamics*, 2nd ed., Applied Mathematical Sciences Vol. 38 (Springer-Verlag, New York, 1992), Chap. III, pp. 174–183.
[58]A. J. Lichtenberg and M. A. Lieberman, *Regular and Chaotic Dynamics*, 2nd ed., Applied Mathematical Sciences, Vol. 38 (Springer-Verlag, New York, 1992), Chap. IV, pp. 258–264.
[59]D. F. Escande and F. Doveil, "Renormalization method for computing the threshold of the large-scale stochastic instability in two degrees of freedom Hamiltonian systems," J. Stat. Phys. **26**, 257 (1981).
[60]B. V. Chirikov, "A universal instability of many-dimensional oscillator systems," Phys. Rep. **52**, 263 (1979).
[61]G. Spizzo and M. Veranda, "Weak chaos in the plasma of a fusion device," in *16th Chaotic Modeling and Simulation International Conference - CHAOS 2023, 13–16 June 2023* (Springer, Heraklion, Crete, Greece, 2023).
[62]G. Spizzo, N. Vianello, R. B. White, S. S. Abdullaev, M. Agostini, R. Cavazzana, G. Ciaccio, M. E. Puiatti, P. Scarin, O. Schmitz, M. Spolaore, and D. Terranova, "Edge ambipolar potential in toroidal fusion plasmas," Phys. Plasmas **21**, 056102 (2014).

[63]Y. Feng, M. Kobayashi, T. Lunt, and D. Reiter, "Comparison between stellarator and tokamak divertor transport," Plasma Phys. Controlled Fusion **53**, 024009 (2011).
[64]G. Spizzo, R. B. White, S. Cappello, and L. Marrelli, "Nonlocal transport in the reversed field pinch," Plasma Phys. Controlled Fusion **51**, 124026 (2009).
[65]G. M. Zaslavsky, *Hamiltonian Chaos and Fractional Dynamics* (Oxford University Press, Oxford, 2005), Chap. XI, pp. 173–186.
[66]T. E. Evans, R. K. W. Roeder, J. A. Carter, and B. I. Rapoport, "Homoclinic tangles, bifurcations and edge stochasticity in diverted tokamaks," Contrib. Plasma Phys. **44**, 235 (2004).
[67]T. E. Evans, "Resonant magnetic perturbations of edge-plasmas in toroidal confinement devices," Plasma Phys. Controlled Fusion **57**, 123001 (2015).
[68]D. Pasqualini, H. Koguchi, G. Spizzo, Y. Yagi, Y. Hirano, P. Martin, and H. Sakakita, "Plasma-wall interaction and locked modes in the toroidal pinch experiment TPE-RX reversed-field pinch," J. Phys. Soc. Jpn. **75**, 023501 (2006).
[69]S. Spagnolo, M. Spolaore, M. Bernardi, R. Cavazzana, S. Peruzzo, M. D. Palma, G. D. Masi, G. Grenfell, N. Marconato, E. Martines, B. Momo, N. Vianello, and M. Zuin, "Design of embedded electrostatic sensors for the RFX-mod2 device," J. Instrum. **14**, C11014 (2019).
[70]B. E. Chapman, A. F. Almagri, J. K. Anderson, D. L. Brower, K. J. Caspary, D. J. Clayton, D. Craig, D. J. D. Hartog, W. X. Ding, D. A. Ennis, G. Fiksel, S. Gangadhara, S. Kumar, R. M. Magee, R. OConnell, E. Parke, S. C. Prager, J. A. Reusch, J. S. Sarff, H. D. Stephens, and Y. M. Yang, "Generation and confinement of hot ions and electrons in a reversed-field pinch plasma," Plasma Phys. Controlled Fusion **52**, 124048 (2010).
[71]A. H. Boozer and G. Kuo-Petravic, "Monte Carlo evaluation of transport coefficients," Phys. Fluids **24**, 851 (1981).
[72]F. Trintchouk, M. Yamada, H. Ji, R. M. Kulsrud, and T. A. Carter, "Measurement of the transverse Spitzer resistivity during collisional magnetic reconnection," Phys. Plasmas **10**, 319–322 (2003).
[73]G. Spizzo, R. B. White, and S. Cappello, "Chaos generated pinch effect in toroidal confinement devices," Phys. Plasmas **14**, 102310 (2007).
[74]R. B. White, *The Theory of Toroidally Confined Plasmas*, 3rd ed. (Imperial College Press, London, 2014), Chap. 9.12, pp. 428–435.
[75]E. Martines, R. Lorenzini, B. Momo, S. Munaretto, P. Innocente, and M. Spolaore, "The plasma boundary in single helical axis RFP plasmas," Nucl. Fusion **50**, 035014 (2010).
[76]D. Terranova, M. Agostini, F. Auriemma, M. Gobbin, G. Marchiori, L. Pigatto, P. Porcu, I. Predebon, G. Spizzo, N. Vianello, P. Zanca, D. Abate, T. Bolzonella, D. Bonfiglio, M. Bonotto, S. Cappello, L. Carraro, R. Cavazzana, P. Franz, R. Lorenzini, L. Marrelli, R. Milazzo, S. Peruzzo, M. Puiatti, P. Scarin, M. Spolaore, E. Tomasina, M. Valisa, M. Veranda, B. Zaniol, and M. Zuin, "RFX-mod2 as a flexible device for reversed-field-pinch and low-field tokamak research," Nucl. Fusion **64**, 076003 (2024).